ADVANCED MATERIALS INTERFACES
Open Access
www.advmatinterfaces.de

Ternary Heterostructures Based on $BaTiO_3/MoO_3/Ag$ for Highly Efficient and Reusable Photocatalytic Applications

*Kevin V. Alex, José P. B. Silva, Koppole Kamakshi, and Koppole C. Sekhar**

This work shows the fabrication of an efficient ternary heterostructure photocatalyst by integrating ferroelectric $BaTiO_3$ (BTO) as the bottom layer, semiconductor MoO_3 as the middle layer and plasmonic silver nanoparticles (Ag NPs) as the top layer, respectively. The $BaTiO_3/MoO_3/Ag$ (BMA) heterostructure exhibits a higher photodegradation and photocatalytic efficiency of 100% for rhodamine B (RhB) dye under a UV–Visible light illumination of 60 min when compared with its binary heterostructure counterparts $BaTiO_3/Ag$ (BA) and MoO_3/Ag (MA). The increased photocatalytic activity in BMA heterostructure is attributed to its enhanced interfacial electric field due to the electric double layer formation at BTO-MoO_3 and MoO_3-Ag interfaces. The higher blueshift in the surface plasmon resonance (SPR) peak observed for the BMA heterostructure clearly indicates an increased electron transfer toward the top Ag NPs layer under optical illumination. The higher resistive switching (RS) ratio, the increased difference in voltage minima, and the improved photocurrent generation, as evident from the *I–V* characteristics, illustrate the enhanced charge carrier generation and separation in BMA heterostructure. A smaller arc radius observed for the Nyquist plot of BMA heterostructure clearly showcases its increased interfacial charge transfer (CT). The CT mechanism and reusability of the BMA heterostructure are also studied.

1. Introduction

In recent years, global energy consumption and environmental pollution have been escalating at an alarming rate due to the tremendous hike in population and industrial growth and we are still forced to rely primarily on nonrenewable energy production habits. If the current crisis prevails, very soon the earth will turn into a wasteland. Therefore, it is the need of time for a revolutionary change toward an efficient, renewable, sustainable, and ecofriendly source of energy which can tackle the prevailing energy crisis and environmental pollution. Photocatalysis has grabbed the greater attention of the scientific community since it utilizes the abundantly and naturally available solar energy for the generation of highly reactive free radicals with the aid of a catalyst material. It has diverse applications such as hydrogen fuel production, advanced water treatment, air purification, and bacterial disinfection and hence can be foreseen as an effective solution for most energy and environmental-related issues.[1–4] An efficient photocatalyst requires suitable bandgap energy, higher photogeneration of charge carriers, less recombination, and excellent light harvesting. Among the various strategies, such as morphological tuning, bandgap/strain engineering, and doping, which are employed to improve the photocatalytic performance of semiconductor-based photocatalysts, heterostructure fabrication is seen as an effective strategy for efficiency enhancement due to the formation of interfaces and interfacial field-driven charge carrier separation.[3,5] Our research group has reported that the integration of ferroelectric BTO with semiconductor

K. V. Alex, K. C. Sekhar
Department of Physics
School of Basic and Applied Sciences
Central University of Tamil Nadu
Thiruvarur 610 005, India
E-mail: koppolechandrasekhar@cutn.ac.in

J. P. B. Silva
Physics Center of Minho and Porto Universities (CF-UM-UP)
University of Minho
Campus de Gualtar
Braga 4710-057, Portugal

J. P. B. Silva
Laboratory of Physics for Materials and Emergent Technologies
LapMET
University of Minho
Braga 4710-057, Portugal

K. Kamakshi
Department of Science and Humanities
Indian Institute of Information Technology
Thiruchirapalli, Tamil Nadu India

The ORCID identification number(s) for the author(s) of this article can be found under https://doi.org/10.1002/admi.202201948

DOI: 10.1002/admi.202201948

MoO_3 can result in the formation of an efficient heterostructure photocatalyst with improved performance due to the combined effect of ferroelectric polarization-driven interface charge coupling as well as type-II heterostructure band alignment. The BTO/MoO_3 heterostructure exhibited a higher efficiency of 86% under a UV–Visible light illumination of 60 min for the degradation of rhodamine B (RhB) dye.[6] However, the efficiency of the heterostructure-based photocatalyst still needs to be further improved for commercial applications.

On the other hand, various studies have reported that photocatalytic activity can be enhanced by the incorporation of metal nanoparticles (MNPs) with the parent photocatalyst material, which is coined as "plasmonic photocatalysis."[7,8] Since the MNPs exhibit the surface plasmon resonance (SPR) phenomenon, they can act as efficient visible light harvesters and increase the light-absorbing capacity of the photocatalyst. Furthermore, they can facilitate an efficient charge transfer (CT) mechanism either due to SPR property or by Schottky junction formation.[9] For instance, Zhang et al. fabricated Ag/BTO composite films, which exhibited an efficiency of 62% under 300 min of visible light illumination by using RhB dye.[10] Sinaim et al. studied the photocatalytic performance of the Ag/MoO_3 composite system and reported an efficiency of 94% within 40 min of visible light illumination against RhB dye.[11] Hence, plasmonic heterostructures are projected as highly efficient photocatalysts due to their peculiar features.

Therefore, in this work, we have proposed a novel ternary heterostructure that corresponds to the integration of metal NPs with a ferroelectric-semiconductor heterostructure. These heterostructures can be foreseen as an effective strategy for further improving the photocatalytic efficiency of bilayered heterostructures by utilizing the interfacial electric field from the ferroelectric-semiconductor heterostructure with the plasmonic properties of the metal NPs.[12,13] But such ternary photocatalysts based on ferroelectric and plasmonic materials are studied less in the literature. For instance, Yu et al. fabricated a TiO_2/BTO/Au multilayered coating for photocatalytic antibacterial applications, which exhibited a disinfection efficiency of 94.4% and 98.5%, respectively for *E. coli* and *S. aureus* bacteria under 40 min of exposure to simulated sunlight.[13] Therefore, in the present work, we have integrated green synthesized Ag NPs as a top layer onto the BTO/MoO_3 heterostructure, which is designated as BTO/MoO_3/Ag (BMA). This novel ferroelectric-semiconductor-plasmonic trilayer structure utilizes the ferroelectric polarization of BTO, the semiconducting properties of MoO_3 as well as the plasmonic properties of Ag NPs for a synergistic effect on photocatalytic performance. Furthermore, we have fabricated and studied the photocatalytic activity of bilayer BTO/Ag (BA) and MoO_3/Ag (MA) structures for detailed comparison. Rhodamine B (RhB), a highly poisonous, carcinogenic and polluting dye commonly used in the textile and food sectors, has been chosen as an analyte for testing the photocatalytic activity of different heterostructures.[4,6] The increased photocatalytic activity of BMA heterostructure is explained based on the enhanced interfacial electric field due to the electric double layer formation at BTO-MoO_3 and MoO_3-Ag interfaces.

2. Results and Discussion

2.1. Structural Studies

The X-ray diffraction (XRD) patterns of BA, MA, and BMA heterostructures are shown in **Figure 1**a. The presence of reflections from (101), (006), and (201) lattice planes correspond to the hexagonal crystal structure of silver (JCPDS 41–1402), indicating the formation of Ag NPs.[14] The MA and BMA heterostructures exhibited the reflections corresponding to the (020) peak and are related to the orthorhombic crystal phase (α) of MoO_3. Furthermore, the BA and BMA heterostructures also showed the reflection corresponding to the (101) plane of tetragonal BTO as shown in the inset of Figure 1a.[6] The XRD patterns of all the heterostructures show a preferential orientation along the (101) direction of Ag NPs. The crystallite size (D) is estimated using the Debye–Scherrer Equation (1),

$$D = \frac{0.9\lambda}{\beta \cos\theta} \tag{1}$$

where "λ" is the wavelength of the X-ray, "β" is the full width at half maximum in radians, and "θ" is the diffraction angle of (101) reflection of Ag NPs.[6] The crystallite size is estimated to be 184, 185, and 182 nm, respectively, for the MA, BA, and BMA heterostructure. The scanning electron microscope (SEM) image of the BMA heterostructure depicted the formation of spherical Ag NPs with an average grain size of 255 ± 10% nm. The energy dispersive spectrum (EDS) of the BMA heterostructure is included in Figure 1c. It exhibited all elemental peaks related to BTO, MoO_3, and Ag NPs. The peaks corresponding to C, Na, Mg, and Ca indicated the presence of neem leaf molecules which is the reducing/capping agent for Ag NPs while the Si peak can be attributed to the glass substrate.[15,16]

2.2. Optical Studies

The UV–Visible absorbance spectra of BA, MA, and BMA heterostructures in the wavelength region of 350 to 750 nm are shown in **Figure 2**a. The SPR peak around 450–500 nm range confirmed the formation of Ag NPs in different plasmonic heterostructures.[9,14] Furthermore, the SPR peak is shifted from 473 nm in MA heterostructure to 468 nm in BA heterostructure and to 455 nm in trilayer BMA heterostructure exhibiting a blue shift in the surface plasmon band as depicted in Figure 2b. As per the Drude model, the SPR peak position depends on the effective dielectric constant of the surrounding media and is given by the following mathematical relation (2);

$$\lambda_{SPR}^2 = \lambda_p^2 \left(\varepsilon^{\infty} + 2\varepsilon_{eff}\right) \tag{2}$$

where "λ_{SPR}" is the SPR peak position, "λ_p" represents the metallic bulk plasma wavelength, "ϵ^{∞}" denotes the high-frequency dielectric constant related to interband transitions, and "ϵ_{eff}" represents the dielectric constant of the surrounding media.[17] Since the SPR peak position is inversely proportional to the electron density of the metal core (N) (i.e., $\lambda_{SPR} \propto 1/\sqrt{N}$), the blue shift of the SPR peak in the heterostructures can be attributed to the increase in the electron density in NPs and hence suggests

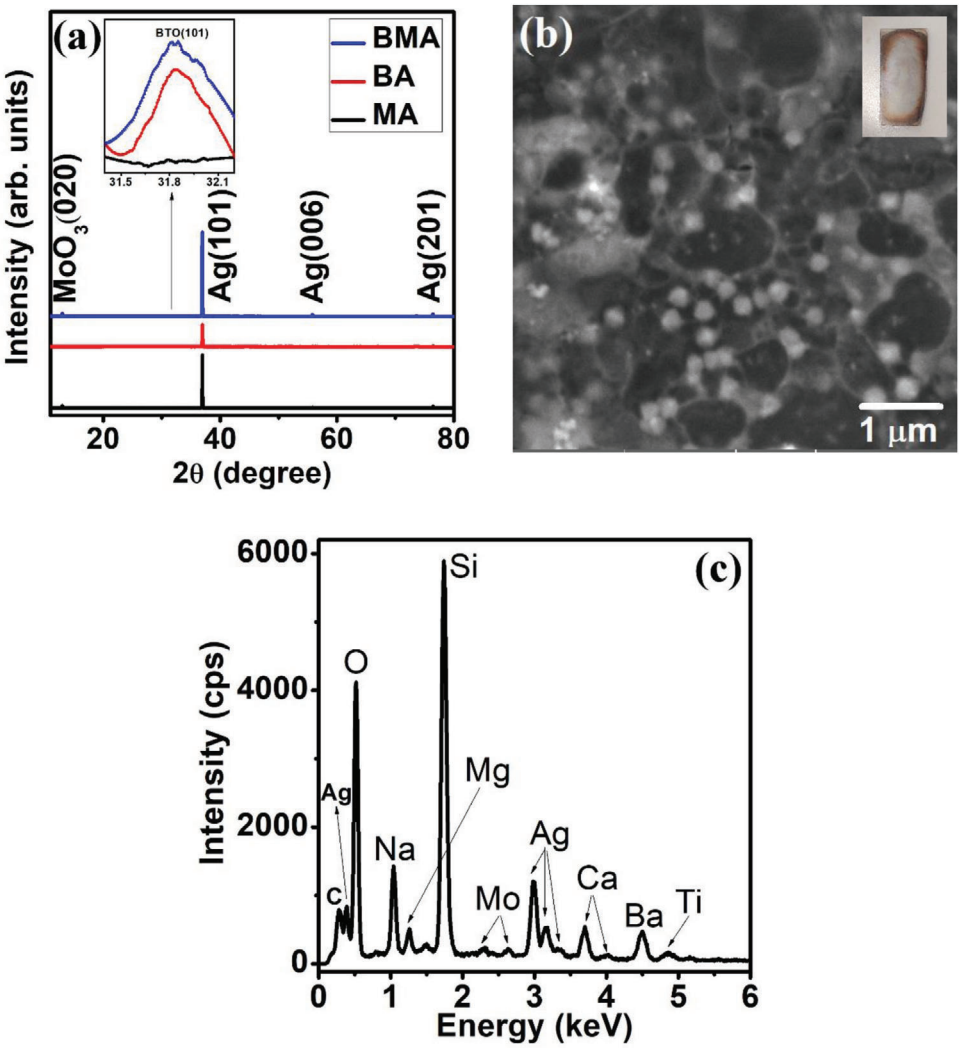

Figure 1. a) X-ray diffraction (XRD) pattern of MoO_3/Ag (MA), $BaTiO_3$/Ag (BA), and $BaTiO_3$/MoO_3/Ag (BMA) heterostructures, b) scanning electron microscope (SEM) image (inset: visual image) of BMA heterostructure, and c) energy dispersive spectrum (EDS) spectrum of BMA heterostructure.

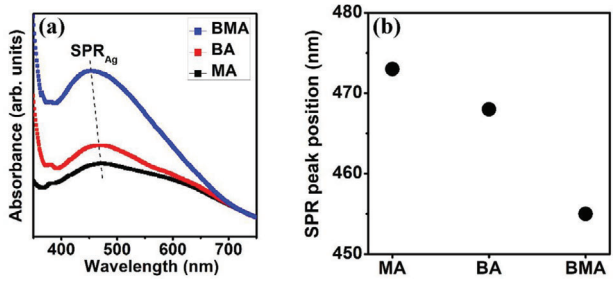

Figure 2. a) Absorbance spectra and b) surface plasmon resonance (SPR) peak position of different heterostructures.

the CT from ferroelectric BTO or semiconductor MoO_3 support layers to the Ag NPs layer under optical excitation.[17,18] The increased electron transfer toward the Ag NPs layer under optical illumination facilitates a higher number of charge carriers for the photocatalytic process. The influence of other factors such as size, shape, and interparticle distance of the NPs which could induce changes in the SPR peak can be neglected here since the deposition conditions of Ag NPs are the same in the fabrication of all heterostructures. This is also supported by the fact that the crystallite size remains almost the same as evident from the XRD analysis.

2.3. Electrical Studies

The current voltage (I–V) characteristics of the heterostructures were studied in the range −3 V to +3 V in order to verify the interfacial electric field and hence the CT mechanism. The semi-log plots between the current and voltage of the heterostructures are depicted in **Figure 3**a. All the heterostructures exhibit non-linear I–V characteristics and resistive switching (RS) effect with a small difference in the minima of forward and reverse voltage cycles.[6,19] The RS ratio, measured at 0.3 V, as well as the difference in voltage minima, is found to be maximum

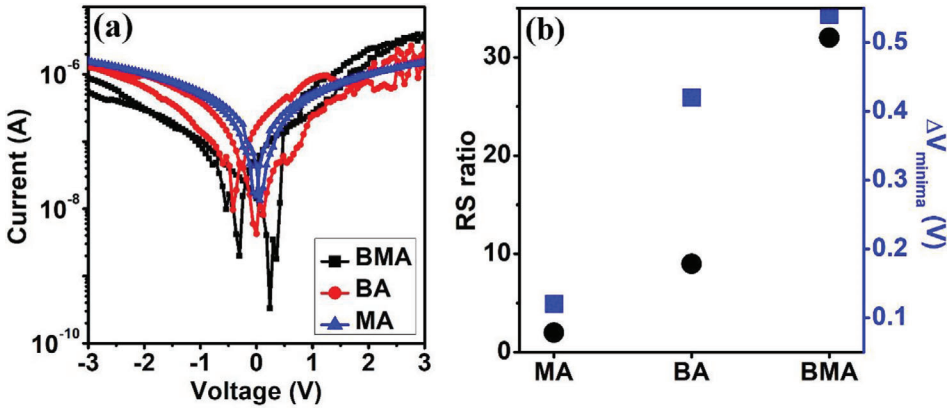

Figure 3. a) *I–V* characteristics and b) restive switching ratio and ΔV_{minima} of different heterostructures.

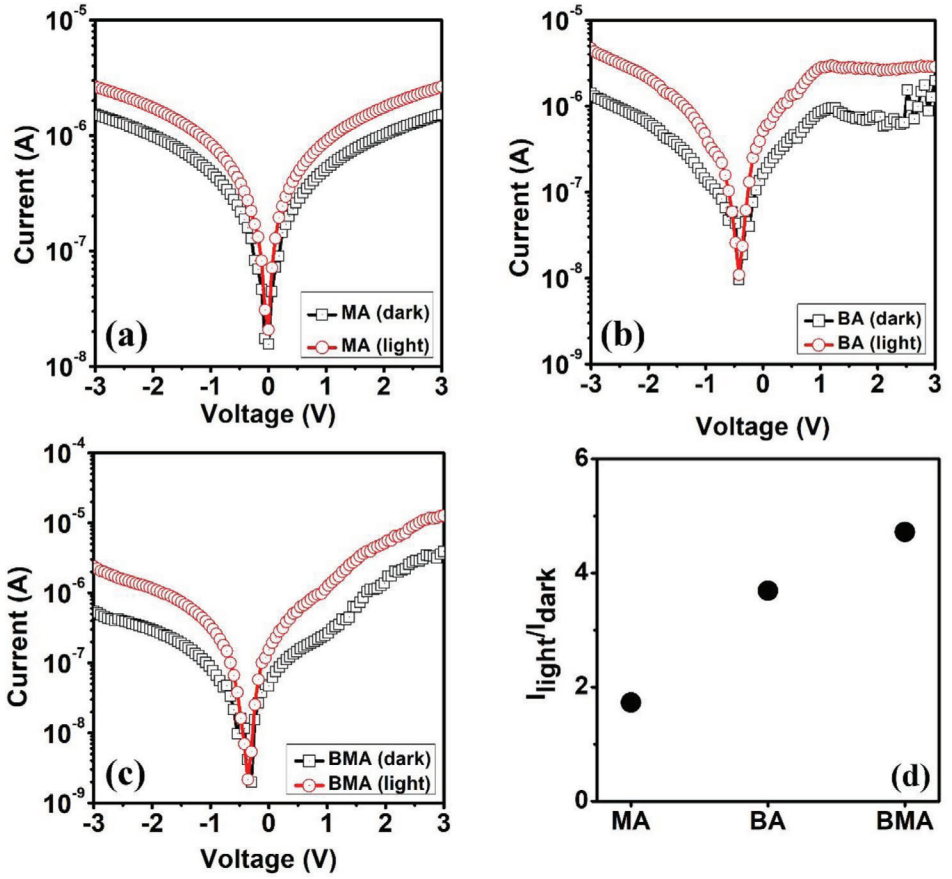

Figure 4. *I–V* characteristics of a) MoO_3/Ag (MA), b) $BaTiO_3$/Ag (BA), c) $BaTiO_3/MoO_3$/Ag (BMA) heterostructures under dark and light conditions, and d) plot of ratio of I_{light}/I_{dark} for different heterostructures.

for the BMA heterostructure, which can be attributed to the enhanced interfacial electric field in comparison with its bilayer counterparts, as seen in Figure 3b.[6] The increased interfacial electric field in BMA heterostructure is due to the formation of an electric double layer at the BTO-MoO_3 interface and MoO_3-Ag interface which will be discussed in detail later.[18]

In order to verify the photogeneration and separation of charge carriers in the heterostructures, the *I–V* characteristics under dark and light conditions were performed and are shown in **Figure 4**a–c. The increase in the current under light illumination indicated the photocurrent generation and hence the photovoltaic (PV) effect in the heterostructures. The ratio of current under the light condition to that under dark condition (I_{light}/I_{dark}) at 1.5 V is found to be higher for the BMA heterostructure as shown in Figure 4d, further confirming its improved charge carrier generation and separation.[20]

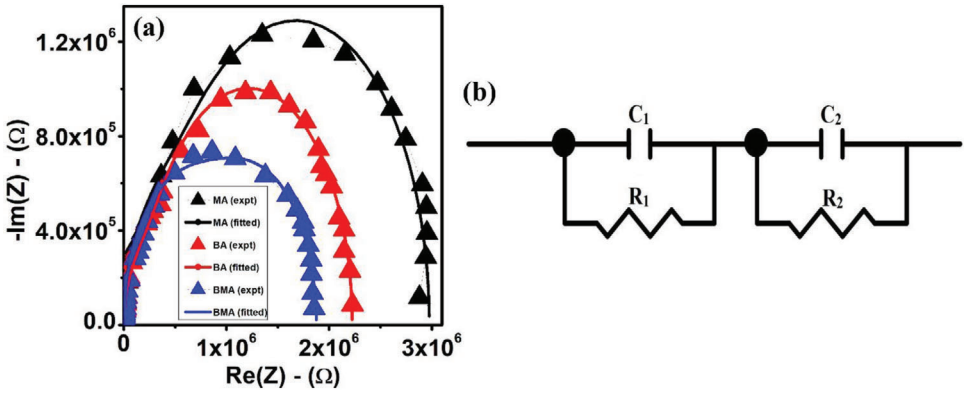

Figure 5. a) Nyquist plot and b) corresponding equivalent circuit of different heterostructures.

Table 1. Fitted parameters of the electrical impedance of the heterostructures.

Samples[	R_1 [Ω]	C_1 [F]	R_2 [Ω]	C_2 [F]
MA	5.50×10^5	6.00×10^{-12}	2.40×10^6	9.80×10^{-12}
BA	2.75×10^5	6.50×10^{-12}	1.95×10^6	1.00×10^{-11}
BMA	8.75×10^5	7.50×10^{-12}	1.00×10^6	3.00×10^{-11}

Furthermore, electrical impedance studies were conducted to understand the CT (or migration) process in the heterostructures. The Nyquist plot of the heterostructures is shown in **Figure 5**a and it is possible to observe that the arc radius is in the order MA > BA > BMA. The smaller arc radius of the BMA heterostructure clearly illustrates its faster interfacial CT and more effective separation of photogenerated charge carriers in comparison with other heterostructures.[21,22] The characteristics of the Nyquist plot can be conceptualized using an equivalent circuit. Typically, the overall impedance of a sample cannot be explained by a single RC network if the Nyquist plot deviates significantly from the semi-circular shape. Since the aspect ratio of the Nyquist plot for all the heterostructures is greater than 2, a minimum of two RC pairs are required to model the equivalent circuit.[23] The Nyquist plot of the heterostructures can be modeled by using two RC pairs in series as shown in Figure 5b and the fitted parameters of the equivalent circuit are tabulated in **Table 1**. Here, R_1 and C_1 represent the bulk part while R_2 and C_2 illustrate the interface effect in the heterostructures.[24] It is clear that the interfacial CT resistance (R_2) is lower in the BMA heterostructure. Furthermore, the interfacial capacitance is also observed to be higher in the BMA heterostructure confirming the enhanced electric field due to the formation of an electric double layer.[18]

2.4. Photocatalytic Studies

The photocatalytic activity of the heterostructures was studied using RhB aqueous solution as the analyte under UV–Visible light exposure for different illumination times (see Figure S1, Supporting Information). The electrons and holes generated in the heterostructures upon the optical illumination take part in the photocatalytic surface reactions. The photocatalytic activity of heterostructures is demonstrated by the decrease in the absorbance of RhB peak at around 570 nm after light illumination, which was determined using the standard Equation (3),

$$\text{Photocatalytic efficiency} = \frac{(A_0 - A)}{A_0} \times 100 \quad (3)$$

where "A_0" and "A" are the peak values of absorbance before and after illumination.[6]

The hypsochromic shift (blue shift) in the absorbance peak of RhB with increasing illumination time revealed the production of its intermediaries, whereas the hypochromic shift (decrease in absorbance peak) in accordance with the illumination time suggested the photodecolorization process involving the breakdown of the chromophore aromatic rings of RhB dye.[6,25] The photocatalytic efficiency, photodegradation, and ratio of absorbance of RhB peak to SPR peak for different heterostructures are plotted as a function of illumination time in **Figure 6**a–c, respectively. The bilayer MA heterostructure exhibited a photocatalytic efficiency of 51.1% and hypsochromic shift of 14 nm in 60 min of UV–Visible illumination, while the BA heterostructure attained a 100% photocatalytic activity within an illumination time of 60 min with negligible hypsochromic shift (≈2 nm) suggesting its weaker degradation efficiency. The trilayer BMA heterostructure exhibited 100% efficiency in 60 min of illumination and an enhanced hypsochromic shift of 46 nm which clearly confirmed its better photodegradation efficiency than its bilayer counterparts. The hypsochromic shift is compared with the literature values and the reaction intermediaries formed during the de-ethylation process of RhB for different heterostructures are listed in **Table 2**.[25] The decrease in the ratio I_{RhB}/I_{SPR} as in Figure 6c clearly denotes the photocatalytic activity of the heterostructures. Furthermore, the reaction rate constant (k) of the photocatalytic process of heterostructures is evaluated by the pseudo-first-order Equation (4) and is shown in Figure 6d.[6] The rate constant of MA, BA and BMA heterostructures is determined to be 0.011, 0.076, and 0.051 min^{-1} respectively.

$$-\ln\left(\frac{A}{A_0}\right) = kt \quad (4)$$

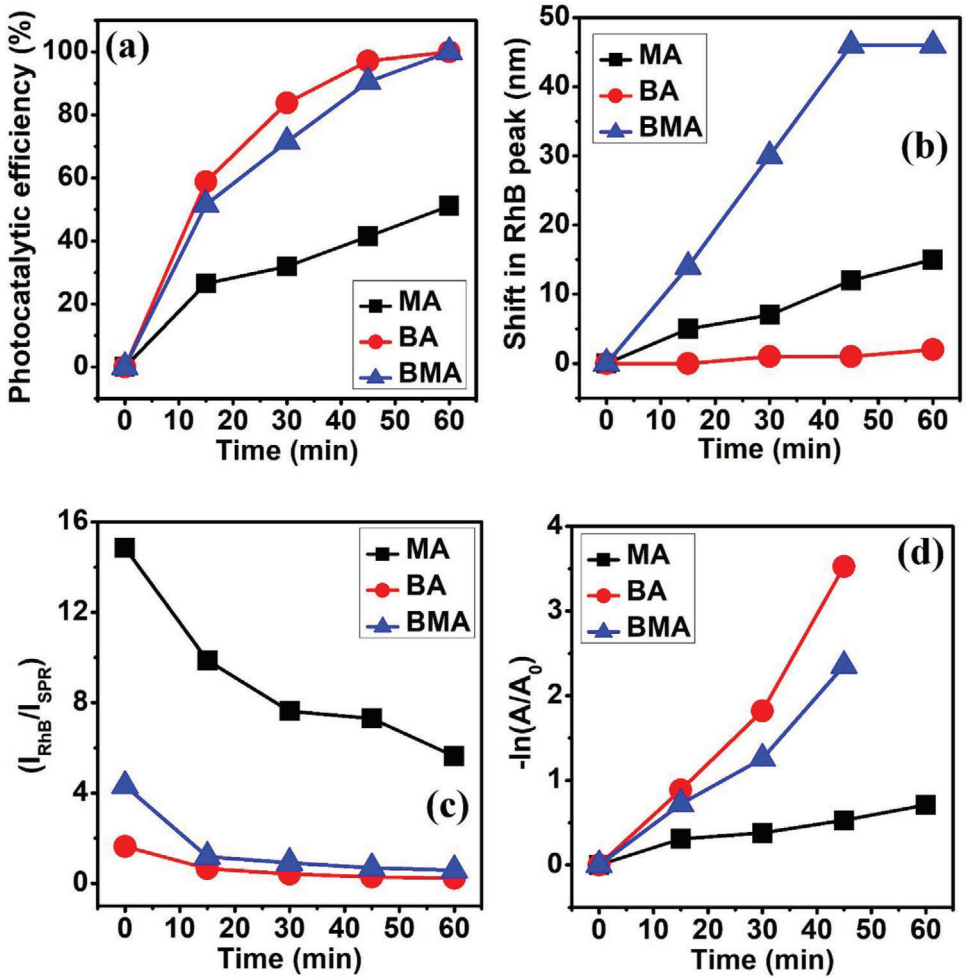

Figure 6. Plot of a) photocatalytic efficiency, b) shift in RhB peak, c) ratio of absorbance of RhB peak to that of surface plasmon resonance (SPR) peak, and d) $-\ln(A/A_0)$ as a function of illumination time.

Table 2. Intermediates formed during photodegradation of RhB at different time intervals.

Illumination time [min]	Intermediates formed after photodegradation		
	MA	BA	BMA
0	RhB	RhB	RhB
15	RhB	RhB	DMRh
30	RhB	RhB	DRh
45	DMRh	RhB	MRh
60	DMRh	RhB	MRh

The photocatalytic activity in plasmonic heterostructures can be mediated by two different CT mechanisms—(i) CT from NPs to the support layer due to SPR (CT_{SPR}), (ii) CT from the support layer to NPs since they can act as electron acceptor or trap (CT_{trap}). These two CT mechanisms can co-exist in the plasmonic heterostructures under UV–Visible illumination.[9,10] Hence, to determine the contribution of SPR of Ag NPs on the photocatalytic activity and CT mechanism involved, the photocatalytic activity of BMA heterostructure was studied under both UV–Visible and visible light (white LED) illumination. **Figure 7** clearly shows that the photocatalytic activity under UV–Visible light illumination is much higher compared to that under visible light suggesting the dominance of CT_{trap} over CT_{SPR} mechanism. Thus, in the BMA heterostructure photocatalyst, the CT_{trap} mechanism from MoO_3 to Ag NPs is found to be dominant over the CT_{SPR} from Ag NPs to MoO_3. In the present work, the contribution of the SPR effect on the photocatalytic activity of plasmonic heterostructure is less, which is contrary to the previously reported work by Zhang et al.[10] They have reported that the CT_{SPR} mechanism dominated over CT_{trap} mechanism in Ag/BTO heterostructure and the photocatalytic activity under visible light was higher than that under UV–Visible illumination. But our results are in accordance with the work reported by Cui et al. which stated that the SPR effect does not have any significant contribution to the photocatalytic activity of Ag-BTO heterostructure and the performance enhancement was attributed to the improved charge carrier separation efficiency due to interface formation.[26]

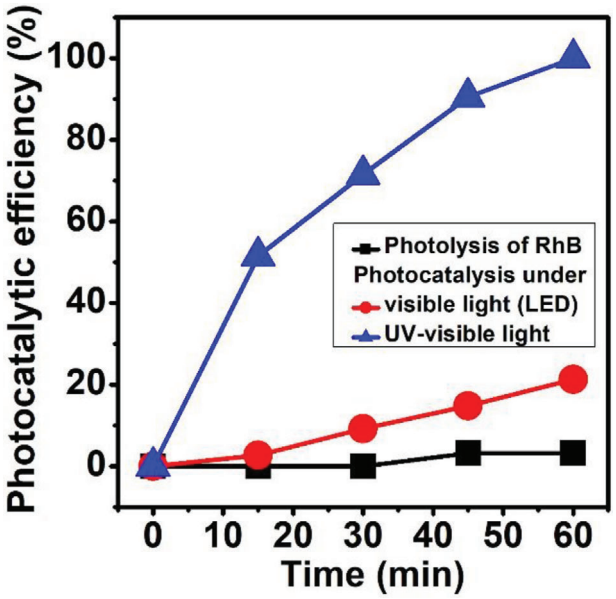

Figure 7. Comparison of photocatalytic efficiency of $BaTiO_3/MoO_3$/Ag (BMA) heterostructure under UV–Visible illumination and visible light and the photolysis of RhB dye.

In order to understand the photocatalytic mechanism in different heterostructures, we have conducted the radical trapping experiment as shown in **Figure 8**. EDTA was employed as a hole scavenger while H_2O_2 was used as an electron scavenger.[27] In the presence of EDTA, the photocatalytic efficiency of BMA heterostructure is observed to be higher than that with dye alone which can be attributed to the fact that EDTA can also become an effective electron donor under UV illumination.[28] The decrease in efficiency in the presence of H_2O_2 confirms that electrons play a major role in the photocatalytic activity of the BMA heterostructure.[6] It is also reported in the literature that a fast degradation of RhB can occur in the presence of H_2O_2 due to the formation of OH* either due to the reaction between photogenerated electrons and H_2O_2 or due to the direct decomposition of H_2O_2 under UV illumination as shown in Equations (5) and (6).[29] Since the photocatalytic efficiency of BMA heterostructure in the presence of H_2O_2 is lower, we can also conclude that the O_2^{-}* radical plays a dominant role over OH* in the photocatalytic process.

$$H_2O_2 + e^- \rightarrow OH^* + OH^- \quad (5)$$

$$H_2O_2 \rightarrow 2OH^* \text{ (under UV illumination)} \quad (6)$$

In the case of BA heterostructure, the photocatalytic efficiency in the presence of EDTA and H_2O_2 is observed to be much lower than that with dye alone. Furthermore, the efficiency of BA heterostructure in the presence of EDTA is lower than that under H_2O_2 suggesting the dominance of holes in the photocatalytic mechanism. In the presence of H_2O_2, the efficiency of BA is found to be 60% lower than that with dye alone which suggests that the OH* radical has least participated in its photocatalytic process.[29] The photodecolorization process in BA heterostructure is found to be higher than that of BMA heterostructure and is due to the photogenerated holes mediated dye degradation mechanism. Here, the photogenerated holes directly degrade the RhB dye rather than indirectly forming the OH* radical.[30,31] The direct interaction between photogenerated holes and RhB molecules leads to the breakdown of its chromophore structure and hence results in the photodecolorization process only.[32] For MA heterostructure, the photocatalytic efficiency in the presence of EDTA is observed to be 7% lower than that with dye alone. Moreover, the activity of MA heterostructure in the presence of H_2O_2 is higher than that with dye alone. Hence, electrons and OH* radicals would play a major role in its photocatalytic mechanism.[6]

The reusability of the BMA heterostructure was evaluated for up to five cycles by illuminating it for 1 h as shown in **Figure 9**. The trilayer heterostructure exhibited 100% efficiency for up to three cycles and gradually decreased further. Even though the reusability of the BMA heterostructure is less than that of the BTO/MoO_3 heterostructure,[6] a complete dye degradation was obtained in BTO/MoO_3 heterostructure in 2 h only while we attained 100% dye removal within 1 h using the BMA heterostructure. The photocatalytic activity of BMA heterostructure is compared with the previously reported works in the literature in **Table 3** and hence it can be concluded that the ternary BMA heterostructure is a highly efficient photocatalyst.

2.5. Modeling of the Charge Transfer Mechanism and Photocatalytic Activity in BMA Heterostructure

In order to further understand the charge coupling and the enhanced photocatalytic performance in the BMA heterostructure, we have schematically represented it under equilibrium condition and under UV–Visible light illumination. The BMA heterostructure consists of the ferroelectric BTO as the bottom layer, semiconductor MoO_3 as the middle layer, and plasmonic Ag NPs as the topmost layer. Since the fermi energy level with respect to the vacuum level of Ag NPs (−4.3 eV) is higher than that of BTO (−5.1 eV) and MoO_3 (−6.3 eV), electrons tend to transfer from BTO to MoO_3 layer as well as from Ag NPs to the MoO_3 layer for attaining the equilibrium condition, as shown in **Figure 10**a.[6,10,13] Thus, two space charge regions are formed at the interfaces of BMA heterostructure resulting in an electric double layer, which led to an enhancement in its interfacial electric field, as shown experimentally from the *I–V* characteristics.[13,18] Under UV–Visible illumination, the photogenerated holes transfer from MoO_3 to BTO while photogenerated electrons move from BTO to MoO_3 due to type-II heterostructure band alignment and the photogenerated electrons in MoO_3 can transfer from MoO_3 toward the Ag NPs layer since Ag NPs act as an electron acceptor or trap, as illustrated in Figure 10b.[6,10,13] It was experimentally confirmed that the CT mechanism from Ag NPs to MoO_3 due to the SPR effect is negligible under UV–Visible illumination and the CT_{trap} is dominant over the CT_{SPR} mechanism in BMA heterostructure. Thus, an improved charge carrier separation efficiency can be easily achieved in the trilayer BMA heterostructure for better photocatalytic activity.

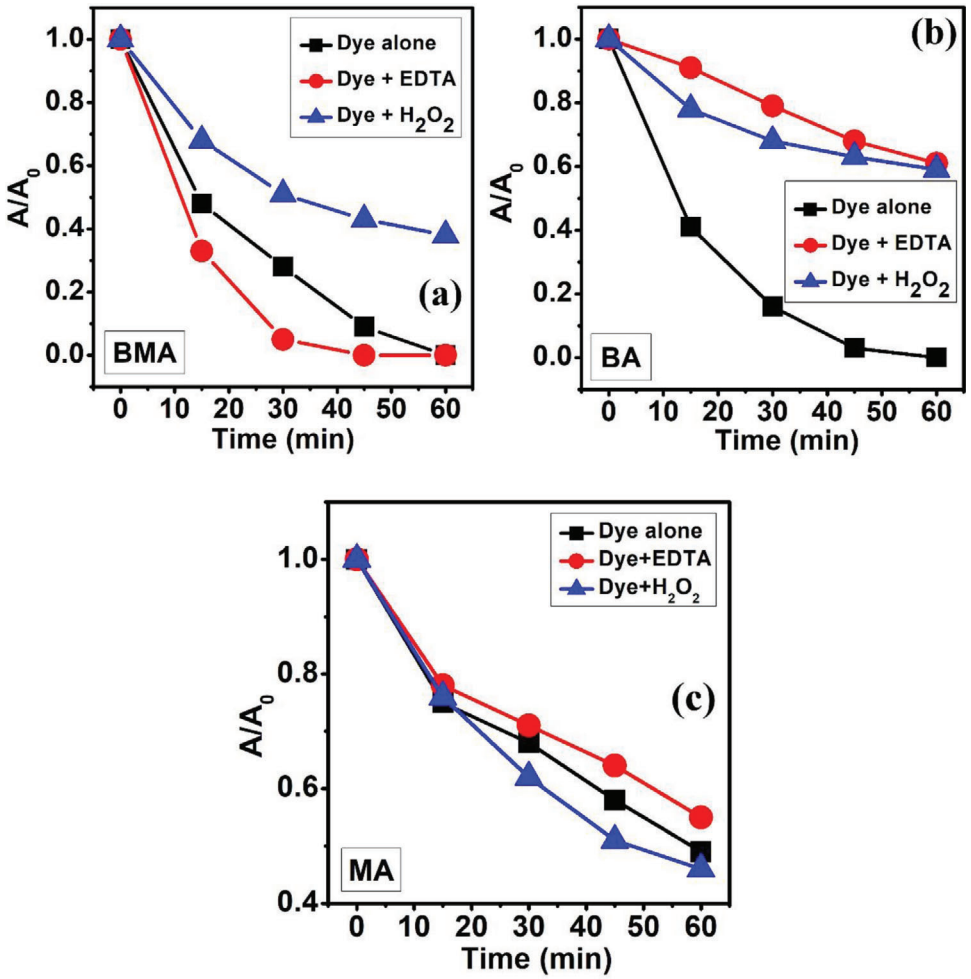

Figure 8. Photocatalytic efficiency of a) $BaTiO_3/MoO_3/Ag$ (BMA), b) $BaTiO_3/Ag$ (BA), and c) MoO_3/Ag (MA) heterostructures in the presence of EDTA and H_2O_2.

The photogenerated electrons in the BMA heterostructure react with the absorbed oxygen molecules to form superoxide radicals (O_2^{-*}) while the photogenerated holes react with the adsorbed water molecules to generate hydroxyl radicals (OH*). These radical species are responsible for the photocatalytic activity of BMA heterostructure in the presence of RhB molecules leading to its decolorization and/or degradation as demonstrated in Figure 10b.[6] It is evident from Figure 10b that the photogenerated electrons transfer toward the topmost Ag NPs layer, which comes in direct contact with the RhB molecules for photocatalytic reactions and hence electrons play a major contribution in the photocatalytic process. This is in accordance with the results observed from radical trapping experiments.

3. Conclusion

We have fabricated a highly efficient ternary heterostructure photocatalyst by combining ferroelectric $BaTiO_3$, semiconductor MoO_3, and Ag NPs and exploring their individual properties. The $BaTiO_3/MoO_3/Ag$ (BMA) heterostructure exhibited a higher photodegradation and photocatalytic efficiency of 100% for rhodamine B (RhB) dye under a UV–Visible light illumination of 60 min when compared with its binary heterostructure counterparts $BaTiO_3/Ag$ (BA) and MoO_3/Ag (MA). The increased efficiency of BMA is attributed to the enhanced interfacial electric field due to the formation of the electric double layer which is experimentally validated through optical and electrical studies. The charge transfermechanism due to electron trap (CT_{trap}) is observed to be dominant over that due to the SPR phenomenon (CT_{SPR}). The photocatalytic activity of BMA heterostructure is found to be stable up to three cycles of reusability. Therefore, this work demonstrated that the integration of ferroelectric, semiconductor and plasmonic materials can be an effective way to achieve highly efficient photocatalysts.

4. Experimental Section

Heterostructures Preparation: The BTO, MoO_3, and green synthesized Ag NPs layers were fabricated over the glass substrate via spin coating technique, spray pyrolysis and drop-casting techniques, respectively. The MA and BA bilayer heterostructures were fabricated by drop-casting green

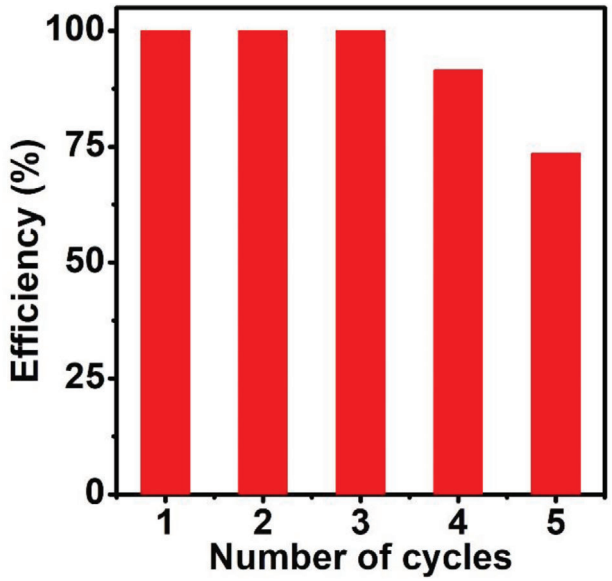

Figure 9. Reusability test of the $BaTiO_3/MoO_3/Ag$ (BMA) heterostructure up to five cycles.

synthesized Ag NPs over MoO_3 film and BTO film, respectively. The BMA heterostructure was prepared by drop casting the green synthesized Ag NPs over the BTO/MoO_3 heterostructure.

Preparation of BTO Layer: The precursor solution was made in two steps using titanium isopropoxide and barium acetate (TIPO). A amount of 1.0955 g of barium acetate was dissolved in 5 mL of acetic acid and the mixture was well agitated at 65 °C for 30 min to form the barium acetate precursor solution. An amount of 1.3 mL of titanium isopropoxide was mixed with 4 mL of 2-methoxy ethanol for an hour to make the TIPO precursor solution. A homogeneous solution was prepared by mixing two precursors and agitated for 1.5 h. On a pre-cleaned glass substrate, a prepared sol of BTO was spin-coated at 2500 rpm with a spin time of 100s, annealed at 600 °C for 2 h and then allowed to cool naturally.

Preparation of MoO_3 layer: By dissolving 0.3087 g of ammonium heptamolybdate tetrahydrate in 25 mL of deionized water and stirring for 30 min, a homogenous precursor solution of 0.01 M was made. Using the ultrasonic spray pyrolysis approach, this solution was sprayed over the surface of the BTO film-coated glass substrate at a temperature (T_S) of 500 °C. Nebulization rate and airflow volume were set at 3 mL min^{-1} and 15 L min^{-1}, respectively. The spray time was set at 5 s in order to obtain desired MoO_3 thickness (t_{MoO_3}). The films were then annealed in the air at 500 °C for 1 h and then allowed to cool naturally to ambient temperature.

Preparation of Ag NPs: Silver nitrate ($AgNO_3$) was used as the precursor and neem leaf extract as the reducing/stabilising agent to prepare the Ag NPs. An amount of 1.5 g of fresh and chopped neem leaves were added to 50 mL of distilled water in a beaker and then heated at 75 °C for 15 min and allowed to cool naturally. The as-prepared solution was allowed to stir for about 24 h and was filtered out to obtain the leaf solution. A amount of 50×10^{-3} M silver nitrate aqueous solution was prepared by adding 0.764 g of silver nitrate into 90 mL of distilled water and then the solution was stirred continuously for 15 min. Further, 10 mL of the freshly prepared leaf solution was added to the as-prepared silver nitrate solution under vigorous stirring at room temperature for about 10 min. The colorless solution now turned into a yellow-brownish solution. Finally, this solution mixture was placed under sunlight for 15 min to obtain Ag NPs. The color change from yellow-brown to dark-drown is an indicator of the formation of Ag NPs. The as-prepared Ag NPs solution was drop cast over the MoO_3 film, BTO film, and BTO/MoO_3 structure to obtain the MA, BA, and BMA heterostructures, respectively.

Characterization of the Heterostructures: The microstructure of the heterostructures was studied using the X-ray diffractometer (Malvern Pan analytical Empyrean) in the range 10–80° with a step width of 0.02° using CuKα radiation of wavelength 0.154 nm. The surface morphology and elemental composition were analyzed using Tescan Vega 3 SEM. The UV–Visible spectroscopy was performed using Shimadzu UV-1800 spectrophotometer in the wavelength range 350–750 nm. For the electrical measurements, coplanar rectangular silver electrodes (2 × 1 mm) separated by a distance of 1 mm were deposited on the upper surface of heterostructures using DC sputtering technique. The current–voltage (*I–V*) measurements were performed using Keithley 2636B electrometer by sweeping the voltage from −3 to +3 V in the forward direction and vice-versa. The photocurrent studies of the heterostructures were studied in the voltage range −3 to +3 V using a white LED bulb of 3 W (wavelength range: 400 to 800 nm). The electrical impedance measurement of the heterostructures was obtained using the Tonghui TH2826A LCR meter at a bias voltage of 1 V and frequency ranging from 1 kHz to 2 MHz. In order to study the photocatalytic activity of the heterostructures, 0.5×10^{-3} M of rhodamine B aqueous dye solution was used as a template. The RhB solution of 0.5×10^{-3} M was dropped uniformly on the surface of heterostructures, waited for 1 h, and was then placed inside a home-made photoreactor for different illumination times. The reactor consists of a 150 W halogen lamp (wavelength range: 350 to 1000 nm) placed at a distance of 5 cm above the photocatalyst. The absorbance measurements were taken before and after the illumination. Further, the radical trapping and reusability test of the heterostructure was also conducted.

Supporting Information

Supporting Information is available from the Wiley Online Library or from the author.

Table 3. Comparison of present work with previously reported works in the literature.

Catalyst	Analyte used	Type of illumination	Illumination time [min]	Photo catalytic efficiency [%]	Photodegradation	Ref
Ag/BTO	RhB	Visible	300	62.0	No	[10]
Ag-BTO	RhB	UV–Visible	45	100.0	No	[26]
Ag/MoO_3	RhB	Visible	140	94.0	No	[11]
Ag/α-MoO_3	Thiophene	Visible	270	98.3	No	[22]
Fe/graphene/g-C_3N_4	MO	Visible	60	82.0	Yes	[33]
$Ag_2O/AgBr$-CeO_2	RhB	Visible	60	95.6	No	[34]
TiO_2/BTO/Au	*E. coli*	Simulated sunlight	40	94.4	–	[13]
$BTO/MoO_3/Ag$	RhB	UV–Visible	60	100.0	Yes	Our work

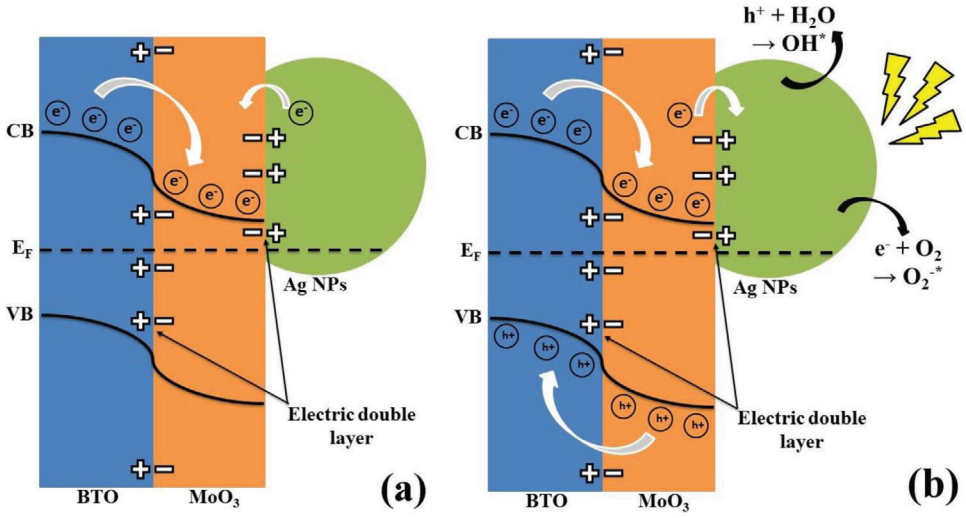

Figure 10. Schematic of $BaTiO_3/MoO_3$/Ag (BMA) heterostructure a) under equilibrium condition and b) under UV–Visible light illumination.

Acknowledgements

K.V.A. acknowledges DST, Govt. of India for the INSPIRE fellowship (IF170601). The authors acknowledge A. Sulthan Ibrahim (Technical Assistant, Dept. of Physics, Central University of Tamil Nadu) for his timely help and support. This work was partially supported by the Portuguese Foundation for Science and Technology (FCT) in the framework of the Strategic Funding Contract UIDB/04650/2020.

Conflict of Interest

The authors declare no conflict of interest.

Author Contributions

J.P.B.S. and K.K. reviewed and edited the work.

Data Availability Statement

The data that support the findings of this study are available in the Supporting Information of this article.

Keywords

ferroelectric, heterostructures, photocatalysis, plasmonic, semiconductors

Received: September 2, 2022
Revised: March 2, 2023
Published online: July 26, 2023

[1] S. Zhu, D. Wang, *Adv. Energy Mater.* **2017**, *7*, 1700841.
[2] R. S. Pedanekar, S. K. Shaikh, K. Y. Rajpure, *Curr. Appl. Phys.* **2020**, *20*, 931.
[3] J. Low, J. Yu, M. Jaroniec, S. Wageh, A. A. Al-Ghamdi, *Adv. Mater.* **2017**, *29*, 1601694.
[4] Y. H. Chiu, T. F. M. Chang, C. Y. Chen, M. Sone, Y. J. Hsu, *Catalysts* **2019**, *9*, 430.
[5] Y. Chen, S. Guerin, H. Yuan, J. O'Donnell, B. Xue, P. Cazade, E. U. Haq, L. J. W. Shimon, S. Rencus-Lazar, S. A. M. Tofail, Y.i Cao, D. Thompson, R. Yang, E. Gazit, *J. Am. Chem. Soc.* **2022**, *144*, 3468.
[6] K. V. Alex, A. Prabhakaran, A. R. Jayakrishnan, K. Kamakshi, J. P. B. Silva, K. C. Sekhar, *ACS Appl. Mater. Interfaces* **2019**, *11*, 40114.
[7] Y. Wang, Y. Chen, Q. Hou, M. Ju, W. Li, *Nanomaterials* **2019**, *9*, 391.
[8] Y. Chen, Y. Wang, W. Li, Q. Yang, Q. Hou, L. Wei, L. Liu, F. Huang, M. Ju, *Appl. Catal., B* **2017**, *210*, 352.
[9] X. Zhang, Y. L. Chen, R. S. Liu, D. P. Tsai, *Rep. Prog. Phys.* **2013**, *76*, 046401.
[10] S. Zhang, B. P. Zhang, S. Li, Z. Huang, C. Yang, H. Wang, *J. Adv. Ceram.* **2017**, *6*, 1.
[11] H. Sinaim, A. Phuruangrat, S. Thongtem, T. Thongtem, *Mater. Chem. Phys.* **2012**, *132*, 358.
[12] Y. Zhang, H. Su, H. Li, Z. Xie, Y. Zhang, Y. Zhou, L. Yang, H. Lu, G. Yuan, H. Zheng, *Nano Energy* **2021**, *85*, 105968.
[13] X. Yu, S. Wang, X. Zhang, A. Qi, X. Qiao, Z. Liu, M. Wu, L. Li, Z. L. Wang, *Nano Energy* **2018**, *46*, 29.
[14] K. V. Alex, P. T. Pavai, R. Rugmini, M. S. Prasad, K. Kamakshi, K. C. Sekhar, *ACS Omega* **2020**, *5*, 13123.
[15] M. S. Sulaiman, *Appl. Res. J.* **2015**, *1*, 265.
[16] A. Baltakesmez, C. Aykac, B. Guzeldir, *Appl. Phys. A* **2019**, *125*, 441.
[17] J. Li, C. Liu, *Eur. J. Inorg. Chem.* **2010**, *2010*, 1244.
[18] V. G. Kravets, F. Wu, T. Yu, A. N. Grigorenko, *Plasmonics* **2022**, *17*, 973.
[19] K. C. Sekhar, J. P. B. Silva, K. Kamakshi, M. Pereira, M. J. M. Gomes, *Appl. Phys. Lett.* **2013**, *102*, 212903.
[20] A. R. Jayakrishnan, K. V. Alex, A. T. Tharakan, K. Kamakshi, J. P. B. Silva, M. S. Prasad, K. C. Sekhar, M. J. Gomes, *ChemistrySelect* **2020**, *5*, 2824.
[21] X. Jiang, H. Wang, X. Wang, G. Yuan, *Sol. Energy* **2021**, *224*, 455.
[22] Y. Zhen, J. Wang, J. Li, M. Fu, F. Fu, Y. Zhang, J. Feng, *J. Mater. Sci.: Mater Electron.* **2018**, *29*, 3672.
[23] I. Matacena, in *2019 15th Conference on Ph.D Research in Microelectronics and Electronics (PRIME)*, IEEE, Piscataway, NJ **2019**, pp. 273–276.
[24] M. Ahmad, M. A. Rafiq, Z. Imran, K. Rasool, R. N. Shahid, Y. Javed, M. M. Hasan, *J. Appl. Phys.* **2013**, *114*, 043710.
[25] F. Chen, J. Zhao, H. Hidaka, *Int. J. Photoenergy* **2003**, *5*, 209.
[26] Y. Cui, J. Briscoe, S. Dunn, *Chem. Mater.* **2013**, *25*, 4215.

[27] J. Yi, C. Bahrini, C. Schoemaecker, C. Fittschen, W. Choi, *J. Phys. Chem. C* **2012**, *116*, 10090.
[28] J. B. Islam, M. Furukawa, I. Tateishi, S. Kawakami, H. Katsumata, S. Kaneco, *SN Appl. Sci.* **2019**, *1*, 1240.
[29] Z. He, C. Sun, S. Yang, Y. Ding, H. He, Z. Wang, *J. Hazard. Mater.* **2009**, *162*, 1477.
[30] M. N. Chong, B. Jin, C. W. K. Chow, C. Saint, *Water Res.* **2010**, *44*, 2997.
[31] U. I. Gaya, A. H. Abdullah, *J. Photochem. Photobiol.* **2008**, *9*, 1.
[32] P. Amornpitoksuk, S. Suwanboon, *J. Alloys Compd.* **2017**, *720*, 582.
[33] Q. Liu, Y. Guo, Z. Chen, Z. Zhang, X. Fang, *Appl. Catal., B* **2016**, *183*, 231.
[34] F. Su, P. Li, J. Huang, M. Gu, Z. Liu, Y. Xu, *Sci. Rep.* **2021**, *11*, 85.